IEEE Access
Multidisciplinary | Rapid Review | Open Access Journal

Received May 15, 2021, accepted June 1, 2021, date of publication June 7, 2021, date of current version June 23, 2021.

Digital Object Identifier 10.1109/ACCESS.2021.3086852

Modelling of Transmission Lines Inside Modern Integrated Semiconductor and Test Boards

MARIUSZ ZUBERT, (Member, IEEE), MARIUSZ JANKOWSKI, ZBIGNIEW KULESZA, AND ANDRZEJ NAPIERALSKI, (Life Senior Member, IEEE)
Lodz University of Technology, 90-924 Lodz, Poland

Corresponding author: Mariusz Zubert (mariusz.zubert@p.lodz.pl)

This work was supported in part by the Polish National Science Centre through the Project OPUS under Grant 2013/11/B/ST7/01742, and in part by the Internal University Grant of the Lodz University of Technology.

ABSTRACT The main purpose of this paper is to present the methodology for calculating the electromagnetic behaviour of real integrated circuit (IC) parts using a no-mesh local Finite Differential Method (FDM). Furthermore, the comparison of computational results and measurements is presented. All considerations are based on typical long transmission lines (TLs) in modern ICs. The obtained results have been analysed in detail and compared with measured values. The measurement data are de-embedded using the test board model. This problem is illustrated in this paper based on a practical example of the Multi-Conductor Transmission Lines test structure whose electrical responses to various excitations are presented and analysed in detail.

INDEX TERMS Integrated circuits, no-mesh FDM, transmission line, microwave, de-embedding, conductor-backed coplanar waveguide.

I. INTRODUCTION

Modelling and analysis of the electromagnetic phenomena occurring in the integrated circuits (ICs) are essential takes for a reliable design of semiconductor microelectronic systems. These tasks are required due to the ongoing trend toward miniaturisation, increasing the operating frequency, and finally design cost reduction of semiconductor microelectronic systems. Therefore, the factors motivating our work are:

- The development of effective modelling and simulation methods, characterised by a nearly linear time complexity for effective simulations of electromagnetic (EM) phenomena inside and around integrated circuit structures and 3D integrated systems.
- The development of a circuit extractor and a computational solver coupled with an electrical simulator, based on the devised modelling and simulation methods, and working with selected IC CAD/CAE software.
- Attempt to develop sets of EM-aware design rules to be used by the software tools analogue to those used during the layout design rule check (DRC), electrical rule check (ERC) and signal integrity test (SI) phases of the design verification.
- The EM solver and circuit extractor verification during the design of the experimental Application Specific Integrated Circuits (ASICs), and analysis of their operation quality.

The first one and the last will be included in the paper based on an example of a designed ASIC test structure and a PCB test board.

II. PREFACE TO COMPUTATIONAL ELECTRO-MAGNETICS

The computational electromagnetics (CEM) is mainly associated with the following three methods – the finite difference time domain (FDTD) method, the method of moments (MoM) and the finite element method (FEM). The electromagnetic model of typical integrated circuits parts with a wideband response has been already presented using the finite difference time domain based on Yee grid [1] for which additional mesh grid points at a half-space point and half-time step are included. The advantages of the FDTD are [2]:

- simple implementation of a full-wave solver (vs MoM and FEM),
- simple implementation of material inhomogeneities (vs FEM),

The associate editor coordinating the review of this manuscript and approving it for publication was Dušan Grujić.

- reasonably accurate geometrical modelling ability (comparable to FEM),
- a single simulation required for a wideband response estimation,
- a perfect implementation of the absorbing boundary conditions (ABC) using the perfectly matched layer (PML).

The main disadvantages of the FDTD method are the following [2]:

- inflexible meshing,
- the problem with precise localisation of the boundary conditions due to Yee grid,
- insufficiency of the FDTD (as MoM) in the case of perfectly conducting radiators and scatters,
- convergence problems in some cases [3].

Additionally, a dense and irregular mesh has to be introduced due to the large aspect ratio of the geometric dimensions (the length and width vs thickness) of paths and layers for integrated circuits structures. This problem can be partially overcome using the following solutions:

- Application of simplified one- and two-dimensional structures of integrated circuits using the one-dimensional lossless transmission line [2] and the multi-conductor, multi-layered transmission lines (MMTL) [4], [5].
- For more complicated 3D integrated structures, an application of the wavelet method based on Haar, Battle-Lemarie [7] and Daubechies [6]. The latter wavelet family turned out to be the best ones. This approach allows three times reduction of the mesh density for each dimension (in relation to the Finite Differential Method), which usually corresponds to 64 × memory reduction and 13 × speed-up of the calculation process [8]. However, a significant difficulty is the need to use one mesh-mod (the smallest space step) coordinated with all geometrical elements (e.g. paths, VIAs and transistors' gate isolation) for the entire analysed structure. Thus, it significantly hinders the simulation of larger fragments of integrated circuits, increasing the computation time and memory occupation.
- The coarse space mesh can be used in the case of the Sampling Biorthogonal time-Domain method (SBTD) [9], [10] instead of the FDTD. Unfortunately, the same resolution (the mesh mode) should be used for the whole domain; therefore, only small structure parts of the integrated circuits can be analysed using this method.

The methods mentioned above allow the modelling of simple structure parts of the integrated circuits. However, employing these approaches can cause a few problems associated with simplifying the geometric structure, problems with the irregular mesh, a large aspect ratio of the geometric dimensions, and one mesh-mod for all dimensions. An adapted method will be presented later in the paper to eliminate the above difficulties. A comparison of the results with the experimental measurements obtained for the MEMS structures will also be presented.

III. ELECTROMAGNETIC MODEL OF THE IC

J. C. Maxwell's curl equations describe the model of electromagnetic phenomena also occurring in the integrated semiconductor circuits. Without loss of generality, we can assume that the electromagnetic wave propagation is in linear, isotropic, non-dispersive, lossy materials. Furthermore, we can also assume that the equivalent magnetic losses are neglected. Therefore, the full-wave Maxwell's equations can be written in the simplified form (1-6) in the Cartesian coordinate system.

$$\frac{\partial E_x}{\partial t} = \frac{1}{\varepsilon}\left(\frac{\partial H_z}{\partial y} - \frac{\partial H_y}{\partial z}\right) - \frac{J_{src,x}}{\varepsilon} - \frac{\sigma}{\varepsilon}E_x \tag{1}$$

$$\frac{\partial E_y}{\partial t} = \frac{1}{\varepsilon}\left(\frac{\partial H_x}{\partial z} - \frac{\partial H_z}{\partial x}\right) - \frac{J_{src,y}}{\varepsilon} - \frac{\sigma}{\varepsilon}E_y \tag{2}$$

$$\frac{\partial E_z}{\partial t} = \frac{1}{\varepsilon}\left(\frac{\partial H_y}{\partial x} - \frac{\partial H_x}{\partial y}\right) - \frac{J_{src,z}}{\varepsilon} - \frac{\sigma}{\varepsilon}E_z \tag{3}$$

$$\frac{\partial H_x}{\partial t} = \frac{1}{\mu}\left(\frac{\partial E_z}{\partial y} - \frac{\partial E_y}{\partial z}\right) \tag{4}$$

$$\frac{\partial H_y}{\partial t} = \frac{1}{\mu}\left(\frac{\partial E_x}{\partial z} - \frac{\partial E_z}{\partial x}\right) \tag{5}$$

$$\frac{\partial H_z}{\partial t} = \frac{1}{\mu}\left(\frac{\partial E_y}{\partial x} - \frac{\partial E_x}{\partial y}\right) \tag{6}$$

where $\vec{E} = [E_x, E_y, E_z]$ - electric vector field components [V/m]; $\vec{H} = [H_x, H_y, H_z]$ – magnetizing vector field components [A/m]; $\vec{J}_{src} = [J_{src,x}, J_{src,y}, J_{src,z}]$ - electric current density vector field components [A/m^2]; ε - permittivity of material [F/m]; μ - magnetic permeability of material [H/m]; σ – electric conductivity of material [S/m].

It should be noted that the *n*-type substrate is used in an integrated semiconductor circuit; therefore, the bottom surface of the substrate is polarised with the lowest possible potential (we assume 0V on the ground plane, see Fig. 1). Thus, all metallic and polysilicon paths (and elements) are biased with positive voltages in relation to the substrate. It results in a greater carrier concentration near the oxide-semiconductor interface than in the bulk of the semiconductor. This is known as the accumulation condition in the Metal-Insulator-Semiconductor capacitor [11]. The equivalent capacitor can describe the capacitance of this

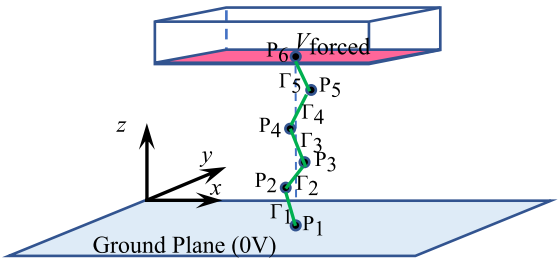

FIGURE 1. The illustration of the shortest path $\Gamma_n, \ldots, \Gamma_1$ connecting the closest points from the polarized mesh point P_n to the bottom ground plate (point P_1). The pointwise enforced voltage V_{forced} condition source implementation refer to the electric vector field components.

element for the accumulation condition. See Sze and Ng [12] (pp. 197-240) and Pierret [11] (pp. 29-64) for a detailed description.

This simplification is also used by Pan [13], Hagness [14], and [15]–[17] for simulations of the IC structures. Notwithstanding, it should be mentioned that this approach cannot be directly used in the case of through silicon via (TSV) elements, where the metal core cannot be polarised as outlined above, and the accumulation condition may not happen in the metal-insulator-semiconductor systems. The detailed model of TSV is discussed in [18]–[21].

A. BOUNDARY AND INITIAL CONDITIONS

There are many models of the boundary conditions used in the computational electromagnetic for radiofrequency and microwave problems. The integrated circuit's bottom ground plane is polarised to zero potential; additionally, the perfect electric conductor is assumed $E_x = E_y = E_z = 0$ and $H_x = H_y = H_z = 0$. The zero-leakage current is assumed in the proposed approach.

All side and top planes are modelled using 2nd-order absorbing boundary conditions (ABCs) for Padé (2,0)/Mur implementation [2], [23], [24], that is:

$$\frac{\partial^2 U}{\partial x \partial t} - \frac{1}{c}\frac{\partial^2 U}{\partial t^2} + \frac{c}{2}\frac{\partial^2 U}{\partial y^2} + \frac{c}{2}\frac{\partial^2 U}{\partial z^2} = 0 \tag{7}$$

for (-)x-direction and $x = x_{\min}$,

$$\frac{\partial^2 U}{\partial x \partial t} + \frac{1}{c}\frac{\partial^2 U}{\partial t^2} - \frac{c}{2}\frac{\partial^2 U}{\partial y^2} - \frac{c}{2}\frac{\partial^2 U}{\partial y^2} = 0 \tag{8}$$

for (+)x-direction and $x = x_{\max}$,

$$E_y = E_z = 0,\ H_y = H_z = 0 \text{ for } x = x_{\min} \text{ and } x = x_{\max} \tag{9}$$

where U is a scalar field component (e.g. E_x, H_x), $x \in \langle x_{\min}, x_{\max}\rangle$ and $c = (\varepsilon\mu)^{-1/2}$ is the wave-phase velocity. The boundary conditions for the y- and z-axis are created analogously.

The initial conditions of electric and magnetising fields are calculated from the steady-state equations derived from the approximated full-wave Maxwell's equations (1-6) by applying $\partial \cdot / \partial t = 0$.

B. INDEPENDENT SOURCES

Three types of independent sources have been implemented in the proposed model: the surface (and pointwise) enforced voltage, the surface (and pointwise) incident wave source condition and the forced conductor current density condition.

The pointwise P_n enforced voltage V_{forced} condition is modelled using the curvilinear integral of an electric vector field $\vec{E}$ evaluated along the shortest path $\Gamma_n, \ldots, \Gamma_1$ connecting the closest points from the polarised mesh point P_n to the nearest point P_1 on the bottom ground plate, see Fig. 1.

$$V_{\text{forced}} = \sum_{i=1}^{n} \oint_{\Gamma_i} \vec{E} \cdot d\vec{s} \tag{10}$$

This integral equation can be approximated using the trapezoidal rule. The algebraic equation (10) is used for modelling of the voltage source V_{forced} as follows

$$\begin{aligned} V_{\text{forced}} \cong\ & \frac{P_{2,x}-P_{1,x}}{2}E_x(P_i) + \sum_{i=2}^{n-1}\frac{P_{i+1,x}-P_{i-1,x}}{2}E_x(P_i) + \\ & + \frac{P_{n,x}-P_{n-1,x}}{2}E_x(P_n) + \frac{P_{2,y}-P_{1,y}}{2}E_y(P_i) + \\ & + \sum_{i=2}^{n-1}\frac{P_{i+1,y}-P_{i-1,y}}{2}E_y(P_i) + \\ & + \frac{P_{n,y}-P_{n-1,y}}{2}E_y(P_n) + \frac{P_{n,z}-P_{n-1,z}}{2}E_z(P_n) + \\ & + \sum_{i=2}^{n-1}\frac{P_{i+1,z}-P_{i-1,z}}{2}E_z(P_i) + \frac{P_{n,z}-P_{n-1,z}}{2}E_z(P_n) \end{aligned} \tag{11}$$

where $\vec{E}(P_i) = [E_x(P_i), E_y(P_i), E_z(P_i)]$ – electric vector field components $[E_x, E_y, E_z]$ at point P_i with coordinates; $[P_{i,x}, P_{i,y}, P_{i,z}]$. The surface enforced voltage source is implemented by applying normalised equation (11) to the considered surface mesh points.

The surface (and pointwise) Incident Wave Source Conditions are implemented only for the vertical electric field component (E_z). It can be modelled as a constant value

$$E_z = E_0 \tag{12}$$

where E_0 is given. The second, more complex model of this source is defined as follows

$$E_z = \begin{cases} 0 & \text{for} \quad t < 0 \\ f(t) & \text{for} \quad 0 \le t < \left(3n_{decay} + n_0\right)t \\ \text{using (3)} & \text{for} \quad \left(3n_{decay} + n_0\right)t \le t \end{cases} \tag{13}$$

where $f(t)$ is defined by one of the formulas:

$$f(t) = E_0 \sin\left(2\pi f_0 \frac{n-n_0}{\Delta t}\right) \tag{14}$$

$$f(t) = E_0 \exp\left(-\left(\frac{n-n_0}{n_{decay}}\right)^2\right) \tag{15}$$

$$f(t) = E_0 \sin\left(2\pi f_0 \frac{n-n_0}{\Delta t}\right) \exp\left(-\left(\frac{n-n_0}{n_{decay}}\right)^2\right) \tag{16}$$

and n – iteration number $n = 1,2,3,\ldots$; Δt - time integration step $\Delta t > 0$; t - time [s]; f_0, n_0, n_{decay} – arbitrary parameters of the incident wave source. using (3) – value is calculated using PDE.

The forced conductor current density condition has been implemented using $\vec{J}_{src}$ the electric current density vector field in the set of equations (1-3) for the selected part of the conductor. In other cases $\vec{J}_{src} = [0,0,0]$.

IV. NUMERICAL SOLUTION

The presented modelling methodology of integrated silicon structures is a handy tool for modelling a passive component.

The active components integration has also been demonstrated in [14]. This part of the paper focuses on effective discretisation and numerical solution of a set of partial differential-algebraic equations (PDAEs).

A. SPATIAL DISCRETISATION

The 3D spatial discretisation of the PDEs is achieved using the non-mesh local Finite Differential Method (FDM) presented in detail in [26]. The main idea of the method mentioned above is to determine the set of differential operators **Du** independently for each point using the second-order Taylor expansion in the 3D space

$$u(P_i) \cong u(P_0) + \sum_{i=1}^{n} \frac{1}{i!} \left(h_i \frac{\partial u}{\partial x} + k_i \frac{\partial u}{\partial y} + l_i \frac{\partial u}{\partial z} \right)^{(i)} \Bigg|_{P_0} \quad (17)$$

where $P_i = [x_0 + h_i, y_0 + k_i, z_0 + l_i]$ for $i = 1, \ldots, n$. The central point P_0 with its neighbourhood $P_1, \ldots P_n$ is the so-called star; see Fig 2. The differential operator $\mathbf{Du}$ can be approximated in the nearest neighbourhood of the point P_0 by the following set of linear equations

$$\begin{bmatrix} h_1 & k_1 & l_1 & \frac{h_1^2}{2} & \frac{k_1^2}{2} & \frac{l_1^2}{2} & h_1k_1 & h_1l_1 & k_1l_1 \\ \vdots & \vdots & \vdots & \vdots & \vdots & \vdots & \vdots & \vdots & \vdots \\ h_i & k_i & l_i & \frac{h_i^2}{2} & \frac{k_i^2}{2} & \frac{l_i^2}{2} & h_ik_i & h_il_i & k_il_i \\ \vdots & \vdots & \vdots & \vdots & \vdots & \vdots & \vdots & \vdots & \vdots \\ h_n & k_n & l_n & \frac{h_n^2}{2} & \frac{k_n^2}{2} & \frac{l_n^2}{2} & h_nk_n & h_nl_n & k_nl_n \end{bmatrix} \cdot \mathbf{Du} == \begin{bmatrix} u_1 - u_0 & \cdots & u_1 - u_0 & \cdots & u_1 - u_0 \end{bmatrix}^T \quad (18)$$

where

$$\mathbf{Du} = \left[\frac{\partial u}{\partial x} \; \frac{\partial u}{\partial y} \; \frac{\partial u}{\partial z} \; \frac{\partial^2 u}{\partial x^2} \; \frac{\partial^2 u}{\partial y^2} \; \frac{\partial^2 u}{\partial z^2} \; \frac{\partial^2 u}{\partial x \partial y} \; \frac{\partial^2 u}{\partial x \partial z} \; \frac{\partial^2 u}{\partial y \partial z} \right]^T \quad (19)$$

This method can be applied for irregular and unbalanced configuration stars. The stability of the differential operator

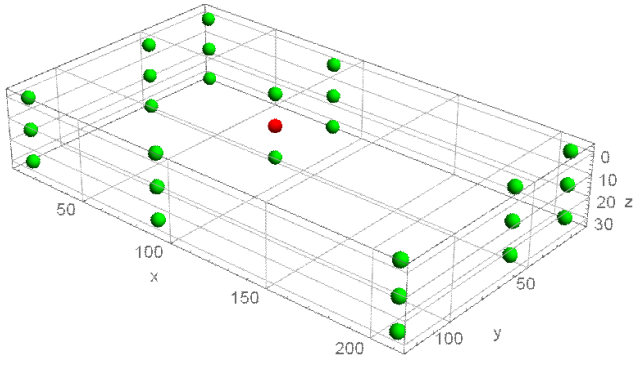

FIGURE 2. The star's configuration: P_0 is the star's centre (the redpoint). Its neighbourhood is presented using green points P_1,...,P_n.

$\mathbf{Du}$ can be obtained by applying normalisation described in equation (23) that normalises the distance between the points as follows:

$P_i = [x_0 + h_i, y_0 + k_i, z_0 + l_i] \rightarrow \hat{P}_i = \left[x_0 + \hat{h}_i, y_0 + \hat{k}_i, z_0 + \hat{l}_i\right]$ for $i = 1, \ldots, n$ and selected value of r.

$$\rho_i = \|P_0 - P_i\| \quad (20)$$

$$\bar{\rho} = \frac{1}{n} \sum_{i=1}^{n} \rho_i \quad (21)$$

$$r = \widehat{\rho}/\bar{\rho} \quad (22)$$

$$\hat{h}_i = rh_i, \hat{k}_i = rk_i, \hat{l}_i = rl_i \quad (23)$$

and finally

$$\mathbf{Du} = \mathbf{T} \cdot \widehat{\mathbf{Du}} \quad (24)$$

$$\mathbf{T} = \left\{ r \quad r \quad r \quad r^2 \quad r^2 \quad r^2 \quad r^2 \quad r^2 \quad r^2 \right\} \quad (25)$$

where $\mathbf{Du}$ - differential operator estimated for $\{P_0, P_1, \ldots, P_n\}$; $\widehat{\mathbf{Du}}$- differential operator estimated for $\{\hat{P}_0, \hat{P}_1, \ldots, \hat{P}_n\}$; $\mathbf{T}$ – normalization vector. A detailed description of the normalisation is presented in [26].

B. MESH GENERATION

Mesh generation is used to reconstruct a continuous geometry space into discrete geometrical and topological cells. Therefore, large geometrically complex objects are approximated using small discrete cells to increase the accuracy of the numerical approximation of the derivatives and integrals during the mesh generation process. The tetrahedron, pyramid, triangular prism, hexahedron, and polyhedron geometry element are most often used in 3D space. These elementary object types are closely related to the numerical method used for solving the differential or integration problems. The proposed spatial discretisation method belongs to the class of meshless methods. Its means that only points (vertexes) are required (without topological information). Therefore, only the positions of the points' need to be imported from the 3D FEM and FDM software. In the case of the proposed system, a simplified method of mesh points generation is used. The integrated silicon circuit structure geometry is defined as a collection of connected rectangular cuboids (one cuboid for the substrate, one for insulation, etc.). Rectangular cuboids are used for metal and polysilicon paths present inside the IC structure. Ten to twenty discretisation points are generated for each side of the rectangular cuboid (Fig. 3a). The set of generated points is projected on the outer edges of the entire IC body. Additionally, the density of mesh points is smoothed. Moreover, the maximal distance between mesh points should not be greater than $\lambda/10$ - $\lambda/5$, where λ is the propagation wavelength in the given material $\lambda = f_{\max}^{-1} \cdot (\varepsilon\mu)^{-1/2}$ and $f_{\max}$ is the greatest considered frequency. Obtained x-, y-, and z-axes are used to generate discretisation points inside the rectangular cuboids (Fig. 3b).

The mesh-less method implies a more complex algorithm to find balanced stars. Such a complex algorithm of finding

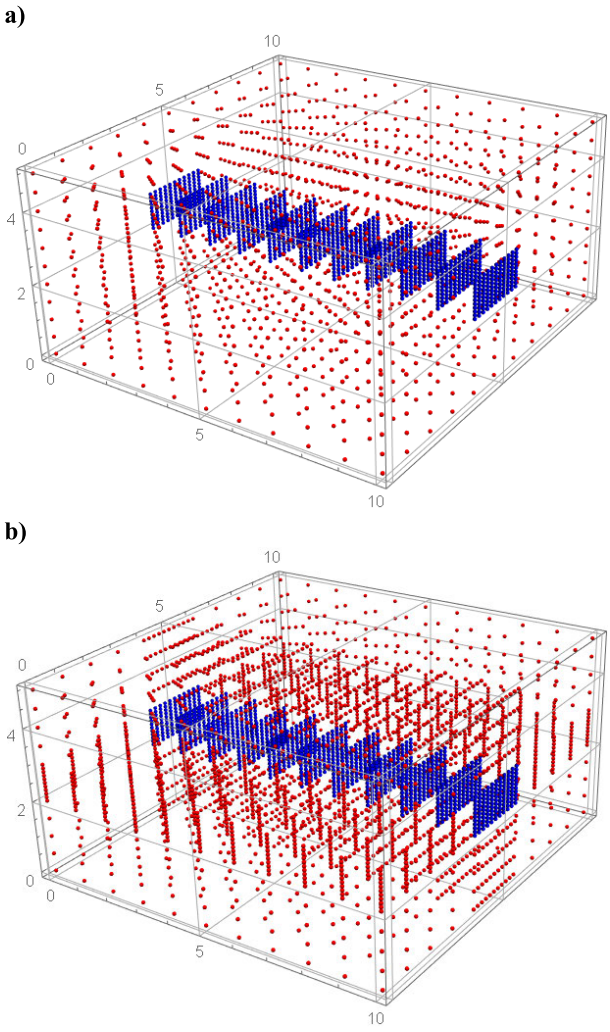

FIGURE 3. Examples of mesh points: a) simplified point generation, b) mesh with points projection on the axes.

already analysed stars was also developed in our computation system. The star configuration cache has been used to speed up the computations. This concept is similar to that used in caching the random access memory. The star configuration and predetermined differential operator **Du** generated for the previously analysed configuration of the stars $\{(h_1, k_1, l_1), \ldots, (h_n, k_n, l_n)\}$ associated with it are stored and effectively used to reduce the computational effort

$$\{n, \bar{\rho}, (h_1, k_1, l_1), \cdots, (h_n, k_n, l_n)\} \rightarrow \mathbf{Du} \tag{26}$$

where redundant values n and $\bar{\rho}$ are used to speed up the searching process.

C. TIME INTEGRATION

The application of the previously presented method of 3D spatial discretisation allows determination of the approximation of the differential operators (Du for given mesh) and a transformation of the problem (including PDEs (1-9) with appropriate boundary conditions (7-9, 11-13)) into the following set of differential-algebraic equations (DAEs)

$$\begin{cases} \dfrac{d\mathbf{V_i}}{dt} = \mathbf{A_{ii}} \cdot \mathbf{V}_i + \mathbf{A_{ib}} \cdot \mathbf{V_b} + \mathbf{Q} \\ \mathbf{B} = \mathbf{A_{ib}} \cdot \mathbf{V_i} + \mathbf{A_{bb}} \cdot \mathbf{V_b} \end{cases} \tag{27}$$

where $\mathbf{V_i}$ – vector containing all dependent variables ($E_x, E_y, E_z, H_x, H_y, H_z$ for given set of mesh points) for which derivatives are present (1-8); $\mathbf{V_b}$ – vector containing all dependent variables ($E_x, E_y, E_z, H_x, H_y, H_z$ for given set of mesh points) for which no derivatives are present (7-9, 11-13); $\mathbf{A_{ii}}$, $\mathbf{A_{ib}}$, $\mathbf{A_{bi}}$, $\mathbf{A_{bb}}$ – coefficients matrixes; $\mathbf{Q}$ - activation vector, e.g. $\overrightarrow{J}_{src}/\varepsilon$ in (1-6); $\mathbf{B}$ – constant terms vector containing independent sources of external stimulation, e.g. (11-13); t – independent variable (time) [s].

This transformation method of a differential problem into DAEs (and equivalent SPICE circuit and Eldo HDL and VHDL-AMS models) has been successfully applied for the analysis of the heat conduction, chemical reactions, as-well-as mechanical applications [25]. In the case of electromagnetic problems, the computational effort is very high. Therefore, we decided to implement the time integration without using external computing solvers (e.g. SPICE, ELDO, etc.). Using the implicit midpoint time integration scheme, we obtained the following system of linear equations to be solved for each iteration time step Δt

$$\begin{bmatrix} \mathbf{1} - \dfrac{\Delta t}{2}\mathbf{A_{ii}} & -\dfrac{\Delta t}{2}\mathbf{A_{ib}} \\ \mathbf{A_{ib}} & \mathbf{A_{bb}} \end{bmatrix} \cdot \begin{bmatrix} \mathbf{V_i}\,(t+\Delta t) \\ \mathbf{V_b}\,(t+\Delta t) \end{bmatrix} = \\ = \begin{bmatrix} \mathbf{1} + \dfrac{\Delta t}{2}\mathbf{A_{ii}} & \dfrac{\Delta t}{2}\mathbf{A_{ib}} \\ \mathbf{0} & \mathbf{0} \end{bmatrix} \cdot \begin{bmatrix} \mathbf{V_i}\,(t) \\ \mathbf{V_b}\,(t) \end{bmatrix} + \\ + \begin{bmatrix} \dfrac{\Delta t}{2}\mathbf{Q}\,(t) + \dfrac{\Delta t}{2}\mathbf{Q}\,(t+\Delta t) \\ \mathbf{0} \end{bmatrix} \tag{28}$$

where $\left[\mathbf{V_i}\,(0)\ \mathbf{V_b}\,(0)\right]^T$ is calculated from (27) for $\mathrm{d}\boldsymbol{V_i}/\mathrm{d}t = 0$

$$\begin{cases} -\mathbf{Q} = \mathbf{A_{ii}} \cdot \mathbf{V_i} + \mathbf{A_{ib}} \cdot \mathbf{V_b} \\ \mathbf{B} = \mathbf{A_{ib}} \cdot \mathbf{V_i} + \mathbf{A_{bb}} \cdot \mathbf{V_b} \end{cases} \tag{29}$$

and given initial conditions (9,12,13). Finally, systems of linear equations (29) and (28) have been solved using SuperLU_MT library.

V. TEST STRUCTURE

The presented theory has been verified using special multiconductor transmission lines (MCTL, Fig. 4) structure used in X-FAB CMOS XDM10 silicon on insulator (SOI) ICs, where n-type substrate is used. The considered structure comprises three Al Si1% Cu0.5%, metal (M3 3 μm $\times$2.3 μm, M2 3 μm $\times$ 0.7 μm and M1 3 μm $\times$ 0.7 μm) and polysilicon (Poly1 3 um $\times$ 0.43 μm) paths, see Fig. 4. The active path M1 or Poly1 is under test. The remaining paths (M3, M2 and Poly1) are terminated using 50 Ω. The length of MCTL structure is $L = 450$ μm, and the total length of M1 in the

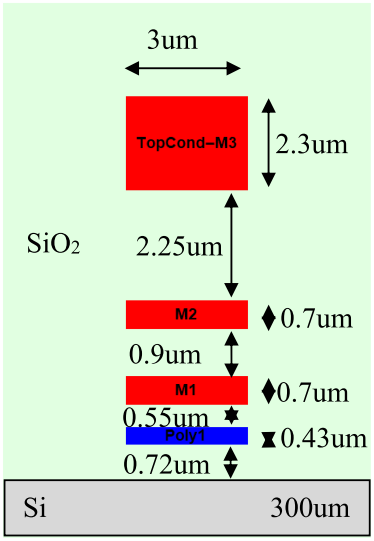

FIGURE 4. The cross-section of multi-conductor transmission lines test structure (not to scale), see also Fig. 5c and Fig. 9a. M1, M2, M3 – metal layers, Poly1 – polysilicon layer.

IC structure is $L_{\text{total}} = 2282\ \mu$m. For simulation, we additionally assume for simulation model SiO_2: $\varepsilon_r = 3.9$, $\tan\delta = 0.0002$; Si: $\varepsilon_r = 12.5$. The simulation of the structure has been performed with frequencies of up to 1 GHz. The entire structure is bonded to a metal core PCB (Fig. 9a, Fig. 5b). The silicon handle wafer has been grounded. All paths (M1, M2, M3, Poly1) are polarised with positive voltages in relation to the substrate. For the electrical characterisation, the biasing current and measurement voltage signals are exchanged with the external circuits via miniature SMA (Fig. 5a).

A. ELECTRICAL ANALYSIS

The electrical behaviour of the analysed IC structure (device under test DUT in Fig. 4b, Fig. 9a) was investigated using the nonlinear Vector Network Analyzer PNA-X Microwave Agilent N5242A de-embedding approach. In the beginning, the electrical reference planes have been moved to the test board connectors presented in Fig. 5a or Fig. 6a using Agilent N4691B Electronic Calibration Module (ECAL). The complex scattering parameters (s_{11}, s_{12}, s_{21}, s_{22}) have to be measured at 32000 spot frequency points (f) distributed from 10kHz to 15GHz. For simplicity, the entire analysis has been performed using chain matrix (ABCD parameters) calculated from the scattering parameters. The connectors ($\mathbf{ABCD}_{\text{connector}}$), Printed Circuit Board (PCB) transmission lines ($\mathbf{ABCD}_{\text{CBCPW}}$) and the interconnections between a PCB and Multi-Conductor Transmission Lines (MCTL) test the IC structure (wire bonding, $\mathbf{ABCD}_{\text{wire-bonding}}$) are eliminated from eq. (30)

$$\begin{aligned}\mathbf{ABCD}_{\text{measurement}} &\approx \mathbf{ABCD}_{\text{connector}} \cdot \mathbf{ABCD}_{\text{CBCPW}} \cdot \mathbf{ABCD}_{\text{wire-bonding}} \\ &\cdot \mathbf{ABCD}_{\text{MCTL}} \cdot \\ &\cdot \mathbf{ABCD}_{\text{wire-bonding}} \cdot \mathbf{ABCD}_{\text{CBCPW}} \cdot \mathbf{ABCD}_{\text{connector}},\end{aligned} \tag{30}$$

in the following way, separately for each frequency (f)

$$\begin{aligned}\mathbf{ABCD}_{\text{MCTL}} &\approx \left(\mathbf{ABCD}_{\text{connector}} \cdot \mathbf{ABCD}_{\text{CBCPW}} \cdot \mathbf{ABCD}_{\text{wire-bonding}}\right)^{-1} \\ &\cdot \mathbf{ABCD}_{\text{measurement}} \\ &\cdot \left(\mathbf{ABCD}_{\text{wire-bonding}} \cdot \mathbf{ABCD}_{\text{CBCPW}} \cdot \mathbf{ABCD}_{\text{connector}}\right)^{-1},\end{aligned} \tag{31}$$

estimated the MCTL structure electrical behaviour; $\mathbf{ABCD}_{\text{connector}}$, $\mathbf{ABCD}_{\text{CBCPW}}$ and $\mathbf{ABCD}_{\text{wire-bonding}}$ are auxiliary chain-estimated in the MCTL structure electrical behaviour; $\mathbf{ABCD}_{\text{connector}}$, $\mathbf{ABCD}_{\text{CBCPW}}$ and $\mathbf{ABCD}_{\text{wire-bonding}}$ are auxiliary chain-matrixes presented in next subsections.

B. THE ELECTRICAL CHARACTERISATION OF THE PRINTED CIRCUIT BOARD TRANSMISSION LINES

The PCBs are manufactured using the FR-4.0 laminate characterised by the following material parameters: dielectric constant 4.58@1 MHz, loss tangent 0.022@1 MHz with copper cladding $t = 35\mu$m. The nominal thicknesses of the dielectric layers are declared as 193 μm, 93 μm and 193 μm for the consecutive layers, respectively. The transmission lines characterisation has been performed for the Conductor-Backed Coplanar Waveguide transmission line (without a top metal cover, CBCPW TL). This transmission line comprises a dielectric substrate with the conductors forming a centre strip ($w = 0.288$ mm) separated by a narrow gap (spacing $s = 0.566$mm) from two semi-infinite ground planes on either side of the top surface (see Z_A-Z_B transmission line in Fig. 5a) and a next ground plane below the mentioned dielectric substrate. It should also be noted that the real effective thickness of the upper dielectric (h) between two cladding coppers is thinner than 193μm by a thickness of the cladding copper and is approximately equal to $h \approx 169.8672\ \mu$m. It should also be emphasised that the radiation losses (α_r) of CBCPW transmission lines are neglected in comparison to conventional microstrip lines [31].

The quasi-static analysis for the characteristic impedance, the effective dielectric constant and the attenuation factor of the CBCPW transmission lines has been performed in [28] (p. 90-97) and [29], [30]. The investigation has been carried out for the CBCPW transmission lines with $L = 55.1$ mm length (the nominal characteristic impedance is $Z_o = 50$ for more, see [28], [29]). This characteristic impedance has also been monitored and tuned during the first analysis of the scattering parameters. The analysis shows that the first resonance frequency is about 1.512 GHz (see Fig. 6b, g and h). This resonance is associated with the length of the transmission line (L) and the dielectric constant, see [43] (pp. 102-118, 151-152, 192, 285-290) and also [34] (p. 7-23), [35]; therefore it will be eliminated from the electrical model. One of the next two resonance frequencies is associated with the microwave behaviour of the SMA connector. This is compared with sample measurements presented in [36] (p.97) and

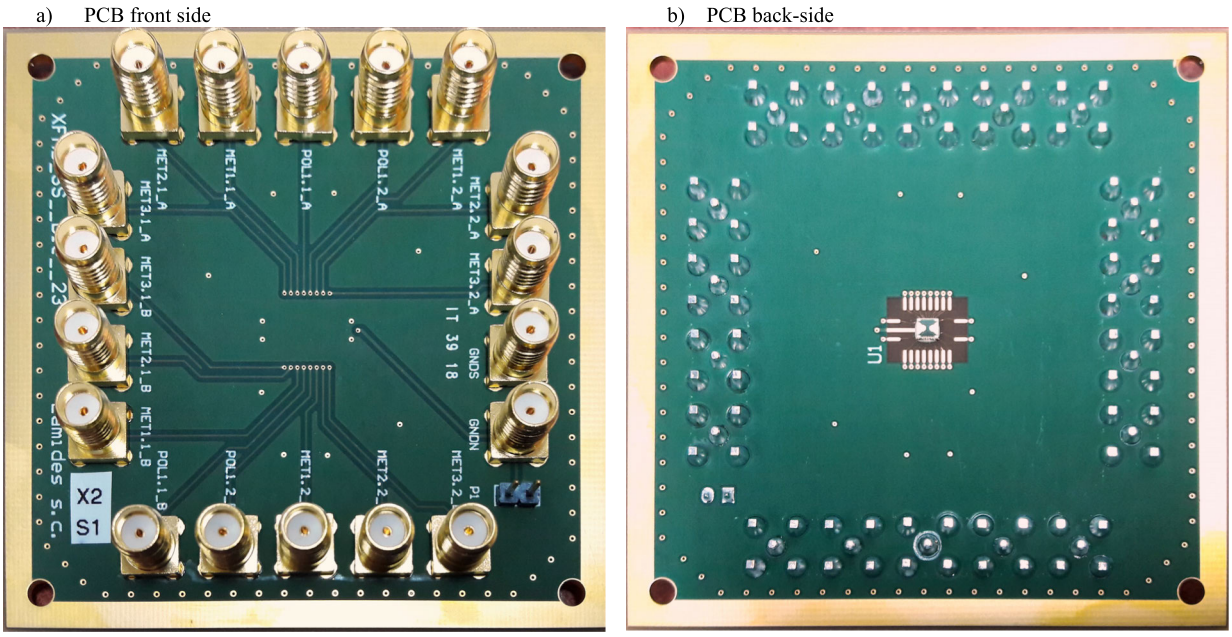

FIGURE 5. The IC test structure (c) is bonded to the test boards. The simplified cross-section of the IC structure has been presented in Fig. 1.

also [37], [38], [41] (p. 204). This and other frequencies are skipped ($\mathbf{ABCD}_{\text{connector}} = \mathbf{1} = [1, 0; 0, 1]$).

The total attenuation factor (α) and phase factor (β) can be obtained from the chain ($\mathbf{ABCD} = [A, B; C, D]$) or scattering ($s_{11}$, s_{12}, s_{21}, s_{22}) measured matrices, using the following equation [42], [43]

$$\begin{aligned}\alpha(f) + i\beta(f) &= \frac{\operatorname{arccosh}(A)}{L}\left[\frac{\text{Np}}{\text{m}} + i\frac{\text{rad}}{\text{m}}\right] \\ &= \frac{(1+s_{11})\cdot(1-s_{22}) + s_{12}s_{21}}{2Ls_{21}}\left[\frac{\text{Np}}{\text{m}} + i\frac{\text{rad}}{\text{m}}\right] \quad (32)\end{aligned}$$

where f is the electric signal frequency in Hertz. Besides, the characteristic impedance (Z_o) can be directly calculated from the following equation for the reference impedance of 50Ω [42], [43]:

$$\begin{aligned}Z_o(f) &= 50\sqrt{\frac{B}{C}}\ [\Omega] \\ &= 50\sqrt{\frac{(1+s_{11})\cdot(1+s_{22}) - s_{12}s_{21}}{(1-s_{11})\cdot(1-s_{22}) - s_{12}s_{21}}}\ [\Omega] \quad (33)\end{aligned}$$

The estimated values of the total attenuation factor, the phase factor and the characteristic impedance are presented in Fig. 6c, d and e. The approximated formulas have been used in the final chain model of the transmission line based on the image parameters [42], [43]:

$$\begin{aligned}&\mathbf{ABCD}_{\text{CBCPW}}(f, L_{new}) \\ &\approx \begin{bmatrix} \cosh\left(\gamma_{\text{approx}}\cdot L_{new}\right) & \text{re}\left(Z_{0,\text{Fitted}}\right)\sinh\left(\gamma_{\text{approx}}\cdot L_{new}\right) \\ \dfrac{\sinh\left(\gamma_{\text{approx}}\cdot L_{new}\right)}{\text{re}\left(Z_{0,\text{Fitted}}\right)} & \cosh\left(\gamma_{\text{approx}}\cdot L_{new}\right) \end{bmatrix} \quad (34)\end{aligned}$$

$$\begin{aligned}&\gamma_{\text{approx}} \\ &= \alpha_{\text{approx}} + i\beta_{\text{Fitted}} \quad (35)\end{aligned}$$

where L_{new} is the length of the CBCPW transmission line on the final board, e.g. $L_{\text{new}} = 28\text{mm}$ for Fig. 5a and $i = (-1)^{0.5}$.

The theoretical calculation of the conductor (α_c) and dielectric losses (α_d) is presented in [30], [29], [43]. Radiation losses (α_r) of microstrip line [30] have been used to simplify the calculation. The theoretically calculated attenuation factor ($\alpha_d + \alpha_c + \alpha_r$) is underestimated for higher frequencies (see Fig. 6c); therefore, the fitted approximation is used;

$$\begin{aligned}&\alpha_{\text{approx}}(f) \\ &= \begin{cases} \alpha_{\text{theoretical}}(f) & \text{for } 0\text{Hz} < f \le 345.601\text{MHz} \\ \alpha_{Fitted}(f) & \text{for } 345.601\text{MHz} \le f \le 3.16\text{GHz} \end{cases} \quad (36)\end{aligned}$$

where the theoretical transmission line model (from [30], [29], [43]) can be written in the simplified form

$$\begin{aligned}\alpha_{\text{theoretical}}(f) &= \alpha_c + \alpha_d + \alpha_r \\ &\approx 0.470076\cdot\sqrt{f\cdot 10^{-9}} \\ &\quad +0.22742822779096295\cdot\left(f\cdot 10^{-9}\right) \\ &\quad +0.0005463682072136707\cdot\left(f\cdot 10^{-9}\right)^2 \\ &\quad \times[\text{Np/m}]. \quad (37)\end{aligned}$$

The fitted polynomial model based on measurements can be written in the following form

$$\alpha_{Fitted}(f) \approx -0.188998\cdot\sqrt{f\cdot 10^{-9}}$$

$$+1.7492 \cdot f \cdot 10^{-9} - 1.44855 \cdot \left(f \cdot 10^{-9}\right)^2 +0.93462 \cdot \left(f \cdot 10^{-9}\right)^3 - 0.290337 \times \cdot \left(f \cdot 10^{-9}\right)^4 +0.0345405 \cdot \left(f \cdot 10^{-9}\right)^5 \left[\text{Np/m}\right]. \quad (38)$$

This estimation has been calculated based on the measurements for the frequency range 283 MHz $\leq f \leq$ 3.16 GHz with the following indicators: $R^2 = 0.999863$, Error Degree Of Freedom EDF = 2746, Error Sum of Squares SSE = 41.59, Pearson χ^2-test of the hypothesis that the residual error is distributed according to the normal distribution and cannot be rejected at the 5% level (statistic 52.6512, P-value 0.202068, see the dotted line in Fig. 6b).

For the frequency range 61 MHz≤f≤1.087 GHz, the approximated model of the phase factor can be estimated from:

$$\beta_{\text{Fitted}}(f) \approx 49.2551 \cdot f \cdot 10^{-9} + -8.00148 \cdot \left(f \cdot 10^{-9}\right)^2 + +11.7971 \cdot \left(f \cdot 10^{-9}\right)^3 + -6.75864 \cdot \left(f \cdot 10^{-9}\right)^4 \text{[rad/m]}, \quad (39)$$

with the following indicators: $R^2 = 0.999999$, EDF = 2187, SSE = 2.01313, The Pearson χ^2 null hypothesis cannot be proven, but the formula is used due to the low residual error, see the dotted line in Fig. 6c.

For the frequency range 61 MHz $\leq f \leq$ 1.087 GHz, the real part of characteristic impedance can be approximated using a rational formula:

$$\begin{aligned}&\text{re } Z_{0,\text{Fitted}}(f) \\ &\approx \{187.773859377139+ \\ &\quad +518.6456558595 \cdot f\, 10^{-9} + \\ &\quad -524.1242030406 \cdot \left(f\, 10^{-9}\right)^2\Big\} / \\ &\quad \Big\{3.9743941670064 + 11.358993679929 \cdot f\, 10^{-9} + \\ &\quad -13.0177611154 \cdot \left(f\, 10^{-9}\right)^2\Big\}\ [\Omega] \end{aligned} \quad (40)$$

with the following indicators $R^2 = 0.999989$, EDF = 2185, SSE = 81.0462, Pearson χ^2 null hypothesis cannot be proven, but this formula is used due to the low residual error, see the dotted line in Fig. 6d.

The additional transmission line discontinuities, bandings and microstrip via holes are neglected but can be considered in equation (30) and (31) based on the formulas presented in [30], [43], [39] and [40].

C. THE ELECTRICAL MODEL OF WIRE BONDING

For long distances (s), the wire bond behaviour is similar to the antenna (see [34]), and at small distances (s) its behaviour is similar to the transmission line. The interconnections between the PCB and the IC structure have been modelled using the following chain matrix of the transmission line:

$$\mathbf{ABCD}_{\text{wire-bonding}}(f, L_{\text{wag}}) \approx \begin{bmatrix} \cosh\left(\gamma_{\text{wag}} \cdot L_{\text{wag}}\right) & Z_{0,wag} \sinh\left(\gamma_{\text{wag}} \cdot L_{\text{wag}}\right) \\ \frac{\sinh\left(\gamma_{\text{wag}} \cdot L_{\text{wag}}\right)}{Z_{0,wag}} & \cosh\left(\gamma_{\text{wag}} \cdot L_{\text{wag}}\right) \end{bmatrix} \quad (41)$$

where L_{wag} is the length of the wire bonding line ($L_{\text{wag}} \approx$ 2.32 mm for Fig. 9a). The characteristic impedance ($Z_{0,\text{wag}}$) can be approximated using the single wire simplified model of a transmission line [36] (pp. 48-51):

$$Z_{0,wag} \approx \frac{138}{\sqrt{\varepsilon_r}} \log_{10} \frac{4s}{d}\ [\Omega] \quad (42)$$

where d is bonding wire diameter $d = 25\mu$m, s is the wire distance above the ground plane $s \approx 0.24$mm, ε_r is the relative dielectric constant of air ($\varepsilon_r \approx 1$). Other more complex models have been presented in [30] and [31] (pp.151-154). The complex propagation constant (γ_{wag}) of a good conductor has been approximated using the following formula [44] (p. 19):

$$\gamma_{\text{wag}} \approx (1+i) \cdot \sqrt{\frac{2\rho}{2\pi f \mu_r \mu_0}} \left[\frac{\text{Np}}{\text{m}} + i\frac{\text{rad}}{\text{m}}\right] \quad (43)$$

where ρ is wire electric resistivity (e.g. $\rho = 2.24 \cdot 10^{-8}\Omega$m for gold [33] (p. 59)), μ_0 is the permeability of vacuum ($\mu_0 = 4\pi \cdot 10^{-7}$ [H/m]), $\mu_r \approx 1$ is the relative permeability of air.

D. THE ELECTRICAL MODEL OF THE MCTL STRUCTURE

The 3D distributed transmission line model has been generated using the approach proposed in section III and IV. The geometric cross-section of the considered MCTL structure been presented in Fig 4. The length of this structure is $L = 450\mu$m, and the total length of each conductor (pad-pad) is about $L_{\text{total}} \approx 228$ 2um. The following material parameters are used for the electrical resistivities: M1 $3.29 \cdot 10^{-8}\Omega$m, M2 $3.11 \cdot 10^{-8}\Omega$m, M3 $3.11 \cdot 10^{-8}\ \Omega$m, Poly $9.68 \cdot 10^{-6}\Omega$m; dielectric constants: SiO_2 3.8, the ground silicon substrate 12.5; and loss tangents: SiO_2 0.0002, substrate 0.02. The M1 path is tested using PNA-X, and all other conductors are terminated (50 Ω) on the test board. The estimated equivalent electric parameters of the MCTL structure for low frequencies are presented in Table 1.

The eddy-current losses (and skin-effect) in a conductor and dielectric losses are strictly related to the fabrication process of the ICs. The eddy-current losses induced by the changing magnetic field cannot be simply analysed using skin depth parameter comparable to the dimension of the path's cross-section. Therefore, the eddy-current losses should be derived and analysed directly using the full-wave Maxwell's equations (1-6). The effective resistance of the path can be estimated from the equation:

$$R = R_{AC} = k_e R_{DC} \quad (44)$$

$$R_{DC} = \rho l / (w\, h) = (l/w)\ R_{\square} \quad (45)$$

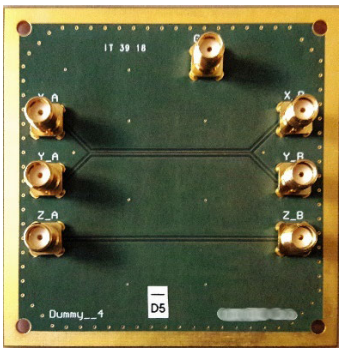

(a)

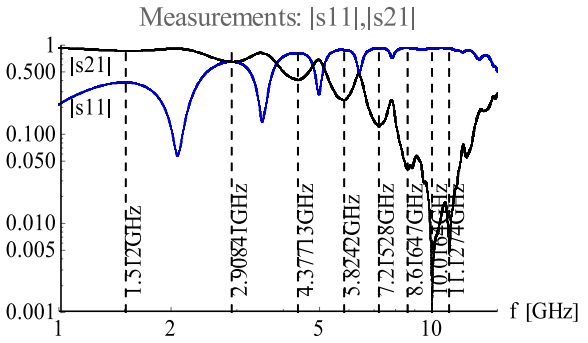

(b)

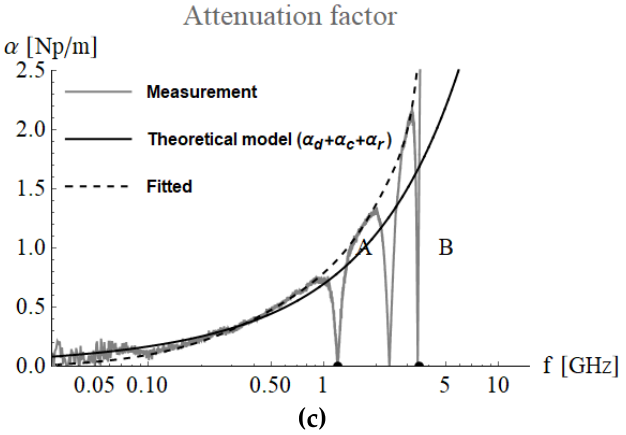

(c)

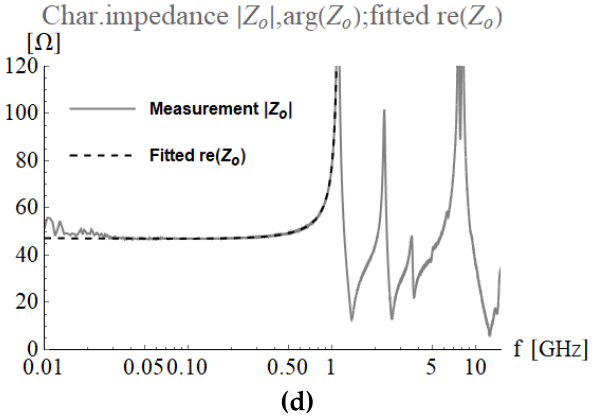

(d)

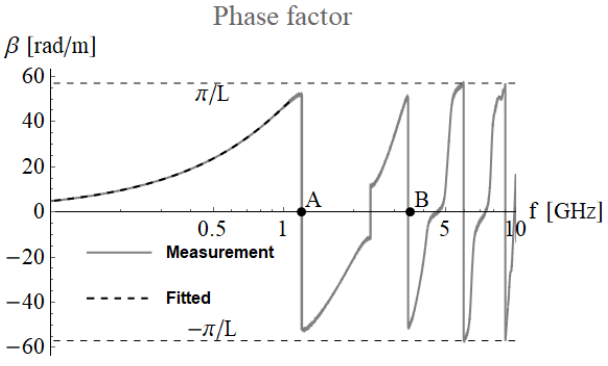

(e)

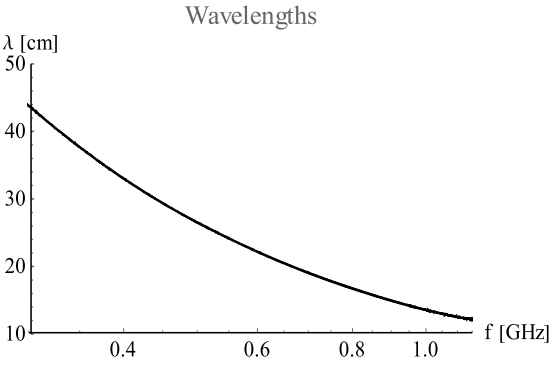

(f)

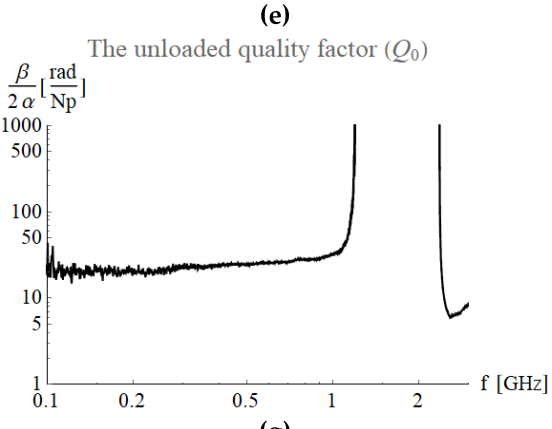

(g)

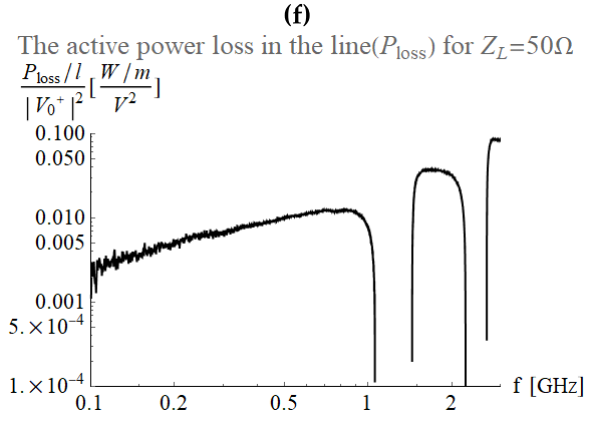

(h)

FIGURE 6. (a) The CBCPW transmission line characterisation board and parameters (L = 55.1mm, w = 0.288mm, s = 0.566mm, $h \approx$ 0.1699mm, t = 35um, ε_r = 4.58, tanδ = 0.022@1MHz). (b) The selected measured parameters. (c) The attenuation factor – measured, theoretical and approximated results. (d) The amplitude of estimated characteristic impedance and approximated real part of characteristic impedance. (e) The phase factor – measured, theoretical results. (f) The measured guide wavelength vs operating frequency. (g) The measured unloaded factor. (h) The active power loss per the unit length of the transmission line.

TABLE 1. The equivalent resistance and inductance of MCTL conductors for low frequencies up to 1 MHz.

Conductor	L=450um	
	Equivalent resistance	Equivalent inductance
M3	2.025 Ω	$5.16{\cdot}10^{-10}$H
M2	6.75 Ω	$5.67{\cdot}10^{-10}$H
M1	7.05 Ω	$5.67{\cdot}10^{-10}$H
Poly	3375 Ω	$5.74{\cdot}10^{-10}$H
Ground	0.00111 Ω	$2.56{\cdot}10^{-10}$H
Equivalent capacitances and mutually coupled inductances: $L_{M1\text{-}Poly}$=$4.85{\cdot}10^{-10}$ H, $L_{M1\text{-}Ground}$=$4.1{\cdot}10^{-1\,1}$H, $L_{Poly\text{-}Ground}$=$4.1{\cdot}10^{-11}$ H, $L_{M2\text{-}M3}$=$3.91{\cdot}10^{-10}$ H, $L_{M1\text{-}M2}$=$4.54{\cdot}10^{-10}$ H, $C_{M1\text{-}M2}$=$4.81{\cdot}10^{-13}$ F, $C_{M2\text{-}M3}$=$3.32{\cdot}10^{-13}$ F, $C_{M1\text{-}Poly}$=$6.79{\cdot}10^{-13}$ F, $C_{M1\text{-}Ground}$=$5.35{\cdot}10^{-13}$ F.		

where R_{DC} is the resistance calculated for the zero frequency; l, w, h – length, height and width of a conductor; $R_{\square}$ - path sheet resistance for a given technology. The eddy-current losses correction coefficient can be estimated from the total resistive heating rate ($\rho E_n^* \cdot E_n$) dissipated in the cross-section of this conductor divided by the total current density (ρE_n)

$$k_e = \frac{\iint\limits_S \rho^{-1} E_n E_n^* dS}{\iint\limits_S \rho^{-1} E_n dS} \tag{46}$$

where $\vec{E}_n$ is electric vector field normal to the considered cross-section S, $\vec{E}_n*$ is the complex conjugate of the complex number of an electric vector field $\vec{E}_n$. A typical distribution of the normalised current density (ρE_n/average(ρE_n)) in the analysed M1 3 μm × 0.7 μm at 10 GHz is shown in Fig 8. In this case, the resistance of the considered path R_{AC} will increase 1.4% at 10 GHz compared to the R_{DC}. A detailed analysis of the results for a wider frequency range is shown in Fig 7. As can be seen, the conductor resistance changes can be neglected within an error of 0.3% in the frequency range of up to 2 GHz. Hence, the skin effect in the path can be neglected in this range. A detailed analytical analysis of skin-effect in classical conductors has been presented in [47].

VI. THE FINAL MCTL MODEL COMPARISON WITH REAL MEASUREMENTS

The low-frequency model equivalent parameters are presented in the previous section. The distributed model comparison with the real measurements is presented in this section.

A. THE SELECTION OF THE COMPARED PARAMETERS

The image propagation constant (γ_{approx}) and the system characteristic impedance ($Z_o(f)$) are excellent for the TL characterisation. They can be directly derived from

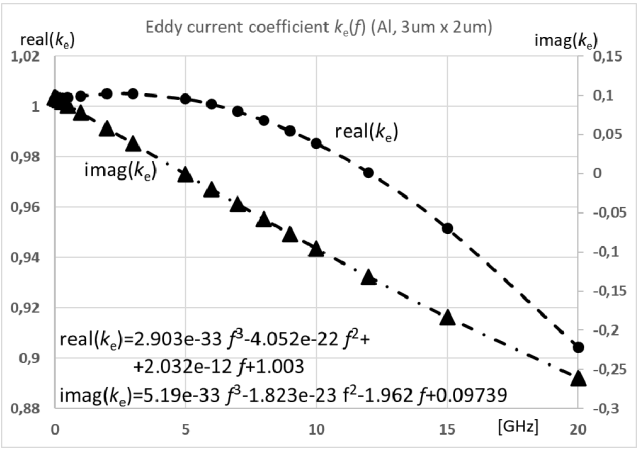

FIGURE 7. The eddy current coefficient k_e of an metal path 3um × 0.7um calculated for 10MHz-20GHz using 2055028 mesh nodes.

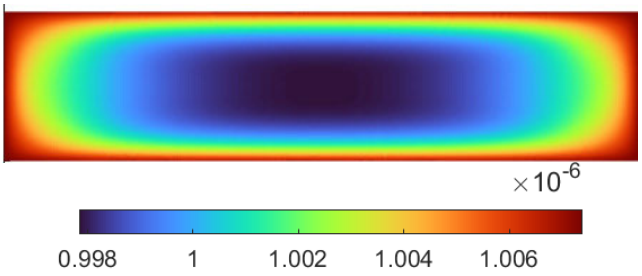

FIGURE 8. The distribution of normalised current density $\rho E/average(\rho E)$ in the cross-section of an active metal path at 10GHz, M1 3um × 0.7um, 2055028 mesh nodes.

equation (33) and (34) only for a physical line dimension (L) is greater than one-twentieth of a wavelength (λ): $L > \lambda/20$, where $\lambda = c \cdot \varepsilon_r^{-1/2}$, $\varepsilon_r \approx 3.8$ is SiO_2 relative permittivity and c is the speed of the electromagnetic wave in a vacuum. In the case of X-FAB ASIC the diagonal and the lower triangular part of the chained matrix are consistent with equation (33, 34) and are satisfied for $f > c/(20L\varepsilon_r^{-1/2}) \approx$ 3.4GHz. Therefore, only the transimpedance element of the de-embedded chained matrix and the scattering matrix elements ($ABCD_{12}$, s_{11}, s_{12}) are used in the final presentation and analysis of the results.

B. THE PRELIMINARY ANALYSIS OF THE TEST BOARDS APPLICABILITY RANGE

The detailed analysis of the measurement circuit PNA X-PCB TL-IC-PCB TL-PNA X (where PCB TL-IC-PCB TL is the path on the IC test board structure in Fig. 5, and PNA X is the network analyser) shows that the best properties of the de-embedded procedure can[will] be acquired for the lowest energy reflection back to the PNA X source terminal at the end of the PCB TL. In this case, the rebound effects are suppressed throughout the measurement test board circuit. Such a situation occurs for the lowest frequencies e.g. 0-100 MHz as well as for the wavelength on the PCB transmission line λ satisfying the following statement

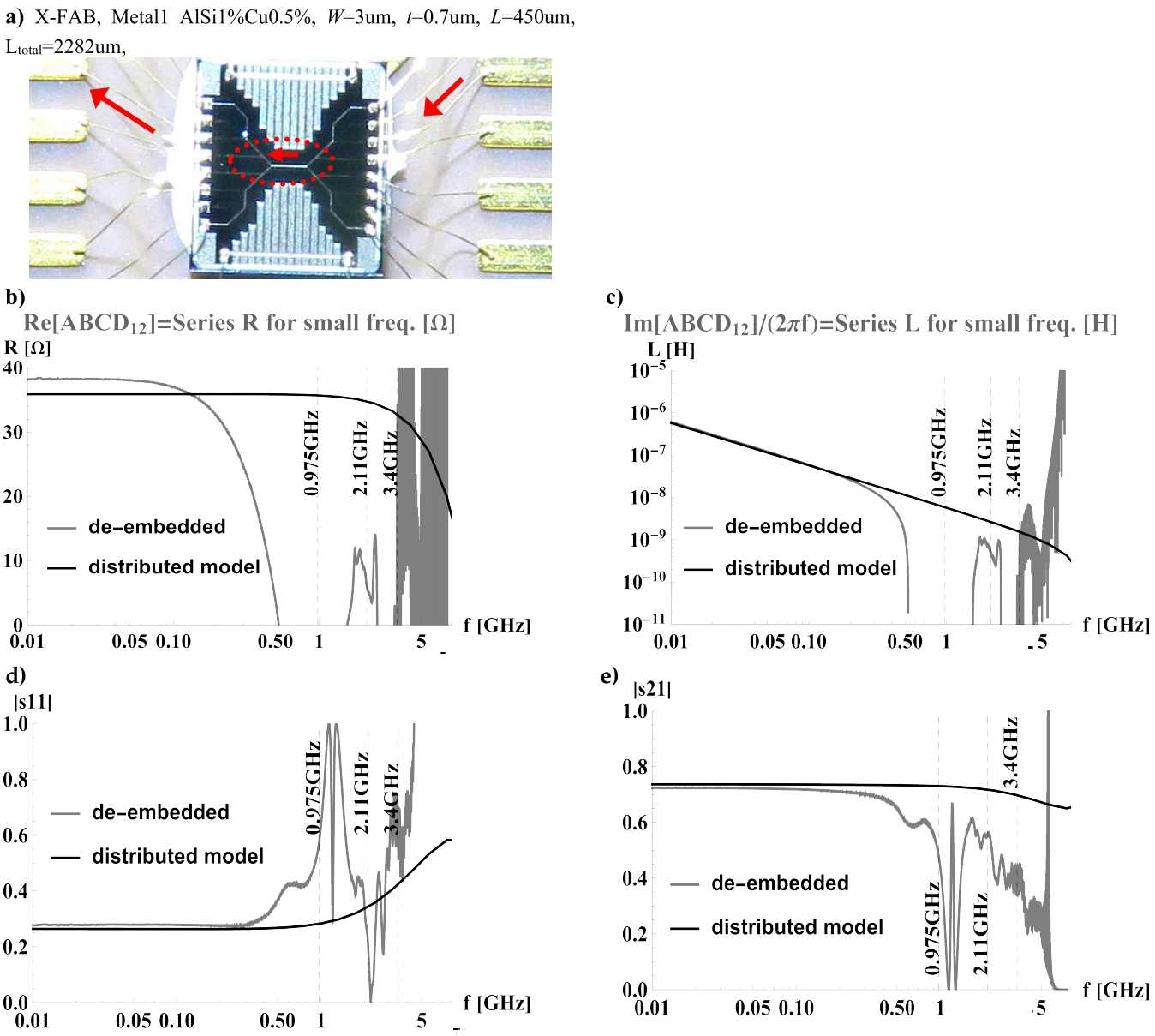

FIGURE 9. The theoretical and measured behaviour of embedded parameters of MCTL test structure: (a) – enlarged microelectronic structure devices manufactured MCTL test structure developed in X-FAB XDM 1um process technology. (b, c) the behaviour of transimpedance parameter, (d, e) the behaviour of scattering matrix elements. The theoretical distributed model of MCTL is presented using grey lines. The behaviour of real IC structure is presented using black lines.

$L \in \{\lambda/4, 3\lambda/4, 5\lambda/4, 7\lambda/4, \ldots\}$, where $\lambda = 2\pi/\beta_{\text{Fitted}}(f)$, and $L \approx 34.7$ mm is the total length of PCB TL between the PNA X and the IC. Afterwards, the de-embedded procedure should be applied for low frequencies and tried in the neighbourhood of 975 MHz, 2.11 GHz, etc. for the PCB test board being developed.

C. THE FINAL MODEL AND REAL IC COMPARISON

The behaviour of the reciprocal system can be effectively and interchangeably described using the chain, and scattering matrix depend on the required application. Therefore, the de-embedding procedure is executed on the chain matrixes by removing of PCB paths and bonding wires. The results are presented in Fig. 9. The transimpedance of M1 conductor ($ABCD_{12}$) is shown in Fig. 9bc and Table 2. The real and imaginary part of this parameter (series R and L) are quite good, estimated up to 200MHz. The reflection coefficient (s_{11}) and the power transferred coefficient (s_{21}) are also correctly estimated up to 200MHz. In addition, the reflection coefficient can also be estimated at 2.11 GHz. However, it is interesting that this frequency cannot be simply used to estimate other parameters. The determined line model cannot be directly used for higher frequencies – the variation of material properties using a multiple-pole Debye, Drude, or Lorentz medium model with polarisation current should be also introduced for this purpose (see also [46]).

TABLE 2. Measured and simulation results written in the estimated function form.

IC	Measurement + de-embedding *PNA-X Microwave Agilent N5242A*	MCTL (distributed) *Proposed distributed model.*	Classical Measurement
X-FAB XDM 1um, M1 with terminated multi-conductor transmission lines Poly1-M1-M2-M3	*Fig. 7b (grey line)* $Re(ABCD_{12})=38.337(\pm0.01513)-4.635(\pm0.471)\cdot10^{-9}\cdot f$ [Ω, Hz] for $10MHz\leq f\leq 50MHz$, $R^2= 0.999998$, SS= 0.218, DOF=84	*Fig. 7b (black line)* $Re(ABCD_{12})=35.86(\pm0.002)-1.1149(\pm0.107)\cdot10^{-10}\cdot f$ [Ω, Hz] for $10Hz\leq f\leq 1.13GHz$, $R^2= 0.(9)$, SS= 0.01468, DOF=63	Series R=38.0 Ω (board#1) 37.6 Ω (board#2) *Digital multimetr: SANWA CD771 (0.3%, current 0.5mA or 1.5mA).*
	Fig. 7c (grey line) $Re(ABCD_{12})=3.234(\pm0.003984)\cdot10^{-8}-2.077(\pm0.0396)\cdot10^{-17}\cdot f$ [H, Hz] for $10MHz\leq f\leq 169MHz$, $R^2= 0.9998$, SS= $3.81\cdot10^{-17}$, DOF=338	*Fig. 7c (black line)* $Re(ABCD_{12})=2.945(\pm0.000424)\cdot10^{-9}-3.998(\pm0.0975)\cdot10^{-20}\cdot f$ [Ω, Hz] for $10Hz\leq f\leq 3.1GHz$, $R^2= 0.(9)$, SS= $7.23\cdot10^{-22}$, DOF=63	-

VII. CONCLUSION

Achievements presented in the paper combine three areas:

- development of an effective modelling and simulation method, with linear time complexity, for fast and accurate simulations of the electromagnetic (EM) phenomena inside and around the IC structures and 3D integrated systems
- building unified dedicated measurement systems for ASICs
- experimental verification of the models and numerical simulations.

The conclusions of their accomplishment are presented in the paper based on an example of the designed ASIC test structure, and the PCB test board are outlined below.

We have developed a dedicated tool for the generation of the distributed electromagnetic models using the set of ODEs as part of our research work (section IV). This tool builds distributed models based on the 3D local no-mesh Finite Differential Method implemented for the first time in the RESCUER software dedicated to a multidomain simulation of the MEMS systems [25]. This method has been applied to solve Maxwell's equations in these studies. Its unique capabilities are the possibility of obtaining a higher approximation level of the PDEs in relation to the number of nodes than the FEM method. This feature is valuable in electromagnetic problems due to increased accuracy of the calculations for smaller numbers of equations or reducing the number of nodes [26].

Moreover, it introduces a more irregular mesh, which is essential in modelling 3D structures and thick gate isolation in modern transistors. Besides, the paper presents the time integration scheme (28) with a relatively low time complexity compared to those used in classic simulators e.g. ANSYS or COMSOL, which significantly impacts problems containing many millions of equations (or nodes). The proposed solution for modelling the through silicon via structures (TSV) requires extending the model with additional electrical dependencies (see discussion in section III).

Another element of the presented work is providing the dedicated test boards with Vector Network Analyzer PNA-X Microwave Agilent N5242A to measure the developed IC for TL (and MCTL) tests using de-embedded techniques (see subsection V.A). We have also tried using multiple plane wave reflections to increase the measurements range for higher frequencies in the neighbourhood of 975 MHz, 2.11 GHz, etc. Promising results were obtained for one parameter only, but overall, this technique does not show promising results (see subsection V.B).

The model and simulation results presented in the paper agreed with the measurement data up to about 200 MHz (sometimes even 500 MHz, see subsection V.C). The measurements show, in principle, an obvious conclusion that the measuring plate must be designed for a specific measuring frequency range, and it is not easy to obtain a very large range of measurement frequencies. Designing dedicated measurement systems for higher frequencies requires better connectors and laminates with the highest isotropic dielectric parameters of the PCB boards. Perhaps a better solution would be to develop the measurement circuit inside the IC, but we wanted to use one technology for different ICs test. The conducted analysis allows empirical confirmation of the numerical models and methods for frequencies of up to 200 MHz (sometimes even 500 MHz). The presented approach can be extended to higher frequencies (e.g., more than 3 GHz) but requires a more accurate description of the dependences of the electrical material parameters of ICs on the applied frequency.

Furthermore, we have presented the results for the designed ICs and PCBs, allowing the analysis of the electromagnetic field distribution in the integrated circuit and the laminate. These studies have been completed and will be published in the future. Our tests have confirmed that the X-FAB technology is very stable and has low leakage currents (see capacitances and mutual inductances parameters in Table 1). We believe that a valuable element of this article is showing a complete characterisation of the PCB and IC as well as the de-embedded procedure that can be applied in practice by engineers and researchers.

REFERENCES

[1] K. Yee, "Numerical solution of initial boundary value problems involving Maxwell's equations in isotropic media," *IEEE Trans. Antennas Propag.*, vol. AP-14, no. 3, pp. 302–307, May 1966.

[2] D. B. Davidson, *Computational Electromagnetics for RF and Microwave Engineering*. 2nd ed. Cambridge, U.K.: CUP, 2011.

[3] M. S. Min and C. H. Teng, "The instability of the Yee scheme for the 'magic time step,'" *J. Comput. Phys.*, vol. 166, no. 2, pp. 418–424, Jan. 2001.

[4] C. Wei, R. F. Harrington, J. R. Mautz, and T. K. Sarkar, "Multiconductor transmission lines in multi-layered dielectric media," *IEEE Trans. Microw. Theory Techn.*, vol. MTT-32, no. 4, pp. 439–449, Apr. 1984.
[5] G.-W. Pan, M. Toupikov, and B. K. Gilbert, "A combined finite difference and analytic expression approach to crossover capacitance in a multilayer dielectric environment," *IEEE Trans. Compon., Packag., Manuf. Technol., B*, vol. 19, no. 3, pp. 615–620, Aug. 1996.
[6] I. Daubechies, "Orthonormal bases of compactly supported wavelets," *Commun. Pure Appl. Math.*, vol. 41, no. 7, pp. 909–996, Oct. 1988.
[7] X. Zhu, G. Lei, and G. Pan, "On application of fast and adaptive periodic Battle–Lemarie wavelets to modeling of multiple lossy transmission lines," *J. Comput. Phys.*, vol. 132, no. 2, pp. 299–311, Apr. 1997.
[8] P. Russer and M. Krumpholz, "The Hilbert space formulation of the TLM method," *Int. J. Numer. Modelling, Electron. Netw., Devices Fields*, vol. 6, no. 1, pp. 29–45, Feb. 1993.
[9] Y. Tretiakov and G. Pan, "Sampling biorthogonal time domain scheme based on Daubechies biorthonormal sampling systems," in *Proc. IEEE Antennas Propg. Int. Symp.*, vol. 4, 2001, pp. 810–813.
[10] G. W. Pan, K. Wang, and B. K. Gilbert, "On multiwavelet-based finite-element method," *IEEE Trans. Microw. Theory Techn.*, vol. 51, no. 1, pp. 148–155, Jan. 2003.
[11] R. F. Pierret, *Modular Series on Solid Devices: Field Effect Devices*, vol. 6, 2nd ed., G. W. Neudeck and R. F. Piereet, Eds. Reading, MA, USA: Addison-Wesley, 1990.
[12] S. M. Sze and K. K. Ng, *Physics of Semiconductor Devices*, 3rd ed. Hoboken, NJ, USA: Wiley, 2007.
[13] G. W. Pan, *Wavelets in Electromagnetics and Device Modeling*. Hoboken, NJ, USA: Wiley, 2003.
[14] S. Taflove and C. Hagness, *Computational Electrodynamics The Finite-Difference Time-Domain Method*, 3rd ed. Norwood, MA, USA: Artech House, 2005.
[15] W. Wójciak, A. Napieralski, M. Orlikowski, and M. Zubert, "Modelling and synthesis of electro-thermal microdevices," in *Mixes Design of Integrated Circuit and Systems*, vol. 5. Norwell, MA, USA: Kluwer, 1998, pp. 77–82.
[16] M. Zubert and A. Napieralski, "RESCUER—The revolution in multidomain simulations—Part I," in *Proc. 22nd Int. Conf. Microelectron.*, May 2000, pp. 549–553.
[17] M. Zubert and A. Napieralski, "RESCUER—The revolution in multidomain simulations. II," in *Proc. 22nd Int. Conf. Microelectron.*, May 2000, pp. 555–559.
[18] K. Salah, Y. Ismail, and A. El-Rouby, *Arbitrary Modeling of TSVs for 3D Integrated Circuits*. Cham, Switzerland: Springer, 2015, doi: 10.1007/978-3-319-07611-9.
[19] K. J. Han, M. Swaminathan, and J. Jeong, "Modeling of through-silicon via (TSV) interposer considering depletion capacitance and substrate layer thickness effects," *IEEE Trans. Compon., Packag., Manuf. Technol.*, vol. 5, no. 1, pp. 108–118, Jan. 2015.
[20] S. Piersanti, F. de Paulis, A. Orlandi, M. Swaminathan, and V. Ricchiuti, "Transient analysis of TSV equivalent circuit considering nonlinear MOS capacitance effects," *IEEE Trans. Electromagn. Compat.*, vol. 57, no. 5, pp. 1216–1225, Oct. 2015.
[21] D.-H. Kim, Y. Kim, J. Cho, B. Bae, J. Park, H. Lee, J. Lim, J. J. Kim, S. Piersanti, F. de Paulis, A. Orlandi, and J. Kim, "Through-silicon via capacitance–voltage hysteresis modeling for 2.5-D and 3-D IC," *IEEE Trans. Compon., Packag., Manuf. Technol.*, vol. 7, no. 6, pp. 925–935, Jun. 2017.
[22] S. Dey and R. Mittra, "Efficient computation of resonant frequencies and quality factors of cavities via a combination of the finite-difference time-domain technique and the Pade approximation," *IEEE Microw. Guided Wave Lett.*, vol. 8, no. 12, pp. 415–417, Dec. 1998.
[23] A. Pozzi, *Application of Pade Approximation Theory in Fluid Dynamics*. New York, NY, USA: World Science, 1994.
[24] G. Mur, "Absorbing boundary conditions for the finite-difference approximation of the time-domain electromagnetic-field equations," *IEEE Trans. Electromagn. Compat.*, vol. EMC-23, no. 4, pp. 377–382, Nov. 1981.
[25] M. Zubert, A. Napieralski, and M. Napieralska, "The application of RESCUER software to effective MEMS design and simulation," *Bull. Polish Acad. Sci. Tech. Sci.*, vol. 49, no. 4, pp. 596–610, Nov. 2001.
[26] M. Zubert, M. Napieralska, and A. Napieralski, "RESCUER—The new solution in multidomain simulations," *Microelectron. J.*, vol. 31, nos. 11–12, pp. 945–954, 2000.
[27] D. Cahill, P. V. Braun, G. Chen, D. R. Clarke, S. Fan, K. E. Goodson, P. Keblinski, W. P. King, G. D. Mahan, A. Majumdar, and H. J. Maris, "Nanoscale thermal transport. II. 2003–2012," *Appl. Phys. Rev.*, vol. 1, Jan. 2014, Art. no. 011305.
[28] C. Dames and G. Chen, "1ω, 2ω and 3ω methods for measurements of thermal properties," *Rev. Sci. Instrum.*, vol. 76, Dec. 2005, Art. no. 124902.
[29] L. Wang *et al.*, *Heat Conduction: Mathematical Models and Analytical Solutions*. Springer, 2008.
[30] R. K. Urlich and W. D. Brown, *Advanced Electronic Packaging*, 2nd ed. Hoboken, NJ, USA: Wiley, 2006.
[31] R. N. Simons, *Coplanar Waveguide Circuits, Components, and Systems*. Hoboken, NJ, USA: Wiley, 2001.
[32] B. C. Wadell, *Transmission Line Design Handbook*. Norwood, MA, USA: Artech House, 1991.
[33] D. M. Pozar, *Microwave Engineering*, 4th ed. Hoboken, NJ, USA: Wiley, 2012.
[34] H.-R. Ahn, *Asymmetric Passive Components in Microwave Integrated Circuits*. Hoboken, NJ, USA: Wiley, 2006.
[35] T. Tong and A. Majumdar, "Reexamining the 3-omega technique for thin film thermal characterization," *Rev. Sci. Instrum.*, vol. 77, no. 10, Oct. 2006, Art. no. 104902.
[36] E. O. Hammerstad, "Equations for microstrip circuit design," in *Proc. 5th Eur. Microw. Conf.*, Sep. 1975, pp. 268–272.
[37] J. Browne, "Broadband amps sport coplanar waveguide," *Microwaves*, vol. 26, no. 2, pp. 131–134, Feb. 1987.
[38] S. Gevorgian, L. J. P. Linner, and E. L. Kollberg, "CAD models for shielded multilayered CPW," *IEEE Trans. Microw. Theory Techn.*, vol. 43, no. 4, pp. 772–779, Apr. 1995.
[39] M. E. Goldfarb and R. A. Pucel, "Modeling via hole grounds in microstrip," *IEEE Microw. Guided Wave Lett.*, vol. 1, no. 6, pp. 135–137, Jun. 1991.
[40] *Microstrip Via Hole Inductance*. Accessed: May 11, 2021. [Online]. Available: https://www.microwaves101.com/encyclopedias/microstrip-via-hole-inductance
[41] R. Sorrentino and G. Bianchi, *Microwave and RF Engineering*. Hoboken, NJ, USA: Wiley, 2010.
[42] V. Székely, "A new evaluation method of thermal transient measurement results," *Microelectron. J.*, vol. 28, no. 3, pp. 277–292, Mar. 1997.
[43] V. Szekely, M. Rencz, A. Poppe, and B. Courtois, "New hardware tools for the thermal transient testing of packages," in *Proc. 3rd Electron. Packag. Technol. Conf. (EPTC)*, Dec. 2000, pp. 46–52.
[44] B. C. Wadell, *Transmission Line Design Handbook*. Norwood, MA, USA: Artech House, 1991.
[45] M. Kirschning, R. Jansen, and N. Koster, "Measurement and computer-aided modeling of microstrip discontinuities by an improved resonator method," in *IEEE MTT-S Int. Microw. Symp. Dig.*, May 1983, pp. 495–497, doi: 10.1109/.MWSYM.1983.1130959.
[46] K. Górecki and P. Ptak, "Compact modelling of electrical, optical and thermal properties of multi-colour power LEDs operating on a common PCB," *Energies*, vol. 14, no. 5, p. 1286, Feb. 2021, doi: 10.3390/en14051286.
[47] N. W. McLachlan, *Bessel Function for Engineers*, 2nd ed. Oxford, U.K.: Clarendon Press, 1955.

MARIUSZ ZUBERT (Member, IEEE) received the Ph.D. degree in electronics from the Lodz University of Technology (TUL), Lodz, Poland, in 1999, and the D.Sc. degree in computer science from the Silesian University of Technology, Gliwice, Poland, in 2011. Since 1999, he has been with the TUL, where he is currently a University Professor. He has authored or coauthored over 100 publications. His research interests include heat transfer problems, VLSI, MEMS, and nano technologies; the multi-domain modeling and simulation of ASIC and SiC PiN Schottky diodes; the design and modeling of ASICs for mobile industry; the real-time monitoring system of high voltage power lines for Ontario Hydro, Kinectrics Inc., for New York City and Ontario One (grant NATO); modeling of electromagnetic interactions in modern (more-than-Moore) 3-D integrated semiconductor structures; the image processing and diagnosis of neurodegenerative diseases, such as BSE—Mad cow disease and Alzheimer; the 3-D ultrastructural amyloid plaque reconstruction and proliferation model using Gaussian hidden Markov random fields; the biometric identification of people using the iris pattern, the automatically translation of multi-physical problems described by PDE/DAEs to hardware description languages, such as VHDL-AMS and HDL-A, and the complex interdisciplinary research, including informatics, electronic, high mathematic, physics and health informatics, and biometrics.

MARIUSZ JANKOWSKI was born in Lodz, Poland, in 1973. He received the M.Sc. and Ph.D. degrees from the Technical University of Lodz (TUL), in 1998 and 2003, respectively. Since 2002, he has been with the TUL, where he is currently an Assistant Professor. His professional activity fields include analysis and design of analog and mixed signal integrated circuits, including high-voltage applications, design of sensors and signal conditioning circuitry for integrated circuits, including 3-D systems and research on electromagnetic properties of analog and mixed signal integrated circuits. His scientific and engineering training include one semester doctoral practice at the University of Gent, Belgium, three month engineering at Atmel premises, Heilbronn, Germany, and one year postdoctoral practice at the Institut Pluridisciplinaire Hubert Curien—IPHC, Strasbourg. He has participated in several Polish and international scientific projects, funded by Polish (the State Committee for Scientific Research, the National Science Centre, the National Centre for Research and Development), and International institutions (EU Framework Programme, ESA). He participated in several commercial contract related to design of mixed-signal high-voltage smart power integrated circuits. In total, he has taken part in design of over ten integrated circuits of various kinds and applications, of which vast majority has been manufactured and proven fully functional. He has authored or coauthored over 60 publications.

ZBIGNIEW KULESZA received the M.Sc. degree in psychology from the Discipline of Electronics, CUL Lublin, in 1991, and the M.Sc. degree in electronics from the TUL Łódź, in 1997. His specialization is in electronic microprocessor and reprogrammable systems in industrial and embedded applications. His fields of professional activity include design of microprocessor systems, microcontrollers, application processors, embedded systems, embedded real-time operating systems, design of on chip and reconfigurable systems, HDL languages in the design of integrated circuits, industrial systems and networks design, data visualization and processing, industrial computers and controllers, industrial networks, and control and data processing systems in industrial electronics, computer design of electronic circuits. His selected achievements, internships, and others include the Gold Medal with distinction for the invention "Holter Recorder With Interchangeable Flash Memory," the 57th World Exhibition of Innovation, Research and Modern Technology—"Brussels Eureka Contest 2008," the Gold Medal for the invention of "Low-noise Holter Recorder with Embedded Cardiogram Analysis," in 2008, the Seoul International Invention Fair, Seoul, in 2008, the Gold Medal for "Virtual Glove," the International Salon of Ideas—Innovations—New Products—IENA 2009, Nuremberg, in 2009, and the Distinction "Łódź Eureka" for "Development of a Vibration Monitoring System for Large Rotor Machines," in 2003.

ANDRZEJ NAPIERALSKI (Life Senior Member, IEEE) was born in Lodz, Poland, in December 1950. He received the M.Sc. and Ph.D. degrees from the Technical University of Lodz, in 1973 and 1977, respectively. The D.Sc. degree in electronics from the Warsaw University of Technology, Poland, in January 1989, and in microelectronics from the Université de Paul Sabatié, France, in May 1989, the Honorary Ph.D. degree of Yaroslaw from Wise Novgorod State University, and the Honorary Ph.D. degree from Gdynia Maritime University, in 2020. From 1973 to 1978, he was with the Institute of Electronics, Technical University of Lodz. In 1983, he joined the Laboratoire d'Automatique et d'Analyse des Systèmes du Centre National de la Recherche Scientifique (LAAS—CNRS), Toulouse, France, where he was working on gold doping influence on the parameters of high-power semiconductor devices. From 1984 to 1985, he was a Lecturer with the Institut des Télécommunications d'Oran, Algeria. From 1985 to 1991, he was a member of the LAAS—CNRS, Research Team on Power Devices, Toulouse, and a Visiting Professor with the Institut National des Sciences Appliquées de Toulouse (INSAT). Since October 1991, he has been a Professor with the Technical University of Lodz. From 1992 to 1996, he was the Vice Director of the Institute of Electronics, and has been the Head of the Department of Microelectronics and Computer Science, since 1996. In 1995, he was a Professor and become a Tenured Professor, in 1999. In 2002, he has been elected and reelected as the Vice Rector for promotion and international co-operation, in 2005. He was invited to many important Universities and Research Centers in Belgium, Denmark, Finland, France, Spain, Switzerland, Italy, U.K., Tunisia, Honduras, Canada, and USA. He gave many lectures and conducted at several laboratories. He supervised 57 Ph.D. theses and six of them received the prize of the Prime Minister of Poland. He is currently a supervisor of over a dozen Ph.D. theses. He participated in eight TEMPUS programs (in three as a coordinator and a contractor), two INCO-COPERNICUS, one ESPRIT, one NATO projects, two projects in the framework of fifth European Program for Research and Technological Development (SEWING IST-2000-28084 and REASON IST-2000-30193), two projects of the Sixth European Program: CARE and PERPLEXUS, three projects of Seventh European Program: EuCARD, EduMEMS, and TIARA, 59 National Research Grants (in 32 as the head of the project), and one Government of Poland expertise (PBZ). He participated in High Energy Physics projects DESY, ITER, ESS, and CERN. He has authored or coauthored over 1170 publications, eight books, 18 textbooks for students, 26 chapters in books, 233 articles in scientific journals (114 in journals from Philadelphia list), 865 papers in conference proceedings, and 17 patents. In 2003, he received the Commander Cross "Merite d'Invention" of the Kingdom of Belgium, Brussels. In 2004, he received the Gold WIPO Medal (World Intellectual Property Organization). In 2008, he received the Medal "Deserved for Russian Federation." Furthermore, he received many National and University awards. In 2012, he received the Distinction of "Merit for Faculty of Microsystem Electronics and Photonics," from the Wroclaw University of Technology. In 2017, he received the Commander Cross of the Order of the Rebirth of Poland. Additionally, he received several medals at the International Exhibitions of Inventions, many awards and honors at Technical University and more than 43 awards and diplomas of Minister. He has also received over 90 awards for his work and scientific research. In 2004, 2006, 2007, 2008, 2009, and 2012, he received the "Lodz Eureka" (two in 2008), and "the Governor Economic Award of Lodz" with the Festival of Science, Technology, and the Arts, in 2007. In 2009, he received with the Team Grand Prix of Innova 2009 at the World Exhibition Brussels Eureka Competition. In 2013, he received the Award from the City of Lodz. From 2000 to 2009, he was appointed as the Chair of the IEEE Poland Electron Devices Chapter. In 2005, he has been elected to the SEFI Administrative Council (Société Européen pour la Formation des Ingénieurs) and as a Polish Representative in this organization. In 2012, he was elected the Chairman of Commission of Electronics and Photonics of URSI and has been nominated to serve as an EDS Region 8 SRC Vice Chair, for the period 2013–2018. He is the Chairman of the Microelectronics Section of the Committee on Electronics and Telecommunication. He was appointed as an Editor of IEEE EDS Newsletter for Scandinavia and Central Europe, from 2001 to 2009. He was an editor of 27 conference proceedings and 13 scientific journals.